Catalysis Science & Technology

Accepted Manuscript

This article can be cited before page numbers have been issued, to do this please use: L. Guo, Q. Zhao, H. Shen, K. Zhang, X. Han, D. Wang, F. Fu and B. Xu, *Catal. Sci. Technol.*, 2019, DOI: 10.1039/C9CY00579J.

ROYAL SOCIETY OF CHEMISTRY

rsc.li/catalysis

Catalysis Science & Technology

View Article Online
DOI: 10.1039/C9CY00579J

ARTICLE

Ultrafine Au Nanoparticles Anchored on Bi_2MoO_6 with Abundant Surface Oxygen Vacancies for Efficient Oxygen Molecule Activation

Received 00th January 20xx,
Accepted 00th January 20xx

DOI: 10.1039/x0xx00000x

Li Guo,[a] Qiang Zhao,[a] Huidong Shen,[a] Xuanxuan Han[a], Kailai Zhang[a], Danjun Wang *[a], Feng Fu*[a] and Bin Xu*[b]

The oxygen molecule activation is one of the most important processes to generate oxygen-containing active free radicals for organic pollutants photocatalytic decomposition. Herein, we demonstrated the ultrafine Au nanoparticles (NPs) anchored on porous Bi_2MoO_6 (BMO) microspheres with rich surface oxygen vacancies (SOVs) planted via a simple chemical reduction-deposition method, could effectively enhance the separation of photogenerated carriers for oxygen molecule activation, and thus more efficient photocatalytic decomposition ability of phenol and dye. The sample (4.0%Au/Bi_2MoO_6) exhibited a remarkable photocatalytic performance for phenol, which is 15 times higher than BMO. The systematic studies indicate that the excellent photocatalytic activity of Au/Bi_2MoO_6 should be ascribed predominantly to the synergistic effect between SOVs, Au NPs and BMO. Both SOVs and Au NPs surface plasmonic resonance (SPR) can not only improve the separation and migration of photogenerated electron (e^-)/hole(h^+) pairs, but also broaden the light responsive spectra, and thereby facilitate the oxygen molecule activation. It also reveals that the photocurrent intensity of 4%Au/BMO sample is approximately 36-fold larger than that of pure BMO, and the ESR signal intensities of $\cdot O_2^-$ and ·OH for Au/BMO exhibit an enhancing tendency compared to pure-BMO, demonstrating that SOVs and Au NPs are responsible for the promoted photocatalytic activity of Bi_2MoO_6 nanostructure. Furthermore, the band gap position of Au/BMO was determined by employing UV-Vis-DRS spectra, VB-XPS and Mott-Schottky plots, thus the enhancement mechanism of oxygen molecule activation is further elucidated.

1 Introduction

For decades, photocatalysis technology has been widely studied to relieve the increasingly serious environmental pollution by utilization of solar energy.[1-6] Generally, oxygen molecule is oxidant in photocatalytic decomposition of pollutants, which can be activated by binding with the photogenerated electron. The superoxide radical ($\cdot O_2^-$), photogenerated hole(h^+) and hydroxyl radical (·OH) are responsible for the decomposition of pollutants. Accordingly, the oxygen molecule activation is one of the most vital processes to generate oxygen-containing radicals for photocatalytic decomposition of the organic pollutants[1-5] and selective organic transformation.[6]

Different from traditional TiO_2-based photocatalysts, bismuth polyoxides such as Bi_2O_3, $BiVO_4$, Bi_2WO_6, Bi_2MoO_6 and $BiPO_4$ have attracted much attention due to their nontoxicity, suitable bandgap and visible light response.[7-13] Among them, Bi_2MoO_6 is a layered Aurivillius-related n-type semiconductor, which consist of alternating $[Bi_2O_2]^{2+}$ and MoO_4^{2-} layers. Owing to its distinguished intrinsic properties,[14-16] Bi_2MoO_6 is considered as a very promising photocatalyst. However, the poor visible-light utilization efficiency, low mobility and rapid recombination of charge carrier still hinder its photocatalytic performance.[17] In this regard, it is highly desirable to find approaches to improve the separation of electrons/hole pairs and broaden the response range of visible light for enhancing the catalytic performance of Bi_2MoO_6-based photocatalysts.[18-20] To this end, the band gap of Bi_2MoO_6 was modulated by controlling its morphology and employing different modification strategies to improve the photocatalytic activity. [21-26]

Defect engineering is an effective strategy to modulate the photocatalytic performance of semiconductors(SC).[27] Oxygen vacancy is an important defect in changing the electronic/optical properties of the photocatalysts, thus improving the photocatalytic performance. Generally, oxygen vacancy is usually introduced through high temperature annealing,[28-30] $NaBH_4$ reduction,[31-33] solvothermal synthesis,[34] ultraviolet radiation and metal ion doping, *etc*.[35,36] It was found that oxygen vacancy can not only led to the reduction of band-gap but also enhance the carrier concentration as a shallow donor, which can extend the light toward longer wavelength, as well as promote the separation of electrons(e^-)/hole(h^+) pairs. On the other hand, noble metal

[a] Shaanxi Key Laboratory of Chemical Reaction Engineering, School of Chemistry and Chemical Engineering, Yan'an University, Yan'an 716000, China. E-mail: wangdj761118@163.com ; E-mail: yadxfufeng@126.com; Tel: +86-911-2332037;
[b] State Key Laboratory of Organic-Inorganic Composites Beijing Key Laboratory of Electrochemical Process and Technology for Materials, Beijing University of Chemical Technology, Beijing 100029, China. E-mail: binxumail@163.com; Tel: +86-10-64434907

†Electronic Supplementary Information (ESI) available. See DOI: 10.1039/x0xx00000x

decoration is another effective modification strategy for photocatalysts.[37-39] The interaction between noble metal nanoparticles (NPs) and SC is expected to form Schottky barriers, which can effectively promote the interfacial electron transfer, and thus significantly prevent the charge carriers recombination.[5,40] Meanwhile, noble metal NPs can respond visible-light owing to the localized surface plasmonic resonance effect (SPR).[41, 42] Among these noble metal NPs, gold (Au) has become the focus for its low toxicity and good environmental compatibility.[43,44]

Although both the noble metal surface deposition and surface oxygen vacancies (SOVs) planting are vital modification strategies for improving photocatalytic activity under visible light,[45] integration the merit of SOVs and noble metal NPs to the surface of semiconductor for synergistic promotion its photocatalytic performance is still a challenge. In this work, we have successfully fabricated Au/Bi_2MoO_6 composites with rich SOVs simultaneous planting via a simple chemical reduction-deposition method, which exhibits superior photocatalytic activity than Bi_2MoO_6. The enhanced photocatalytic efficiency is ascribed to the synergistic effect of SOVs and SPR of ultrafine Au NPs, which improve the oxygen molecule activation process, and thereby it is propitious to generate oxygen-containing radicals for the decomposition of the organic pollutants. This strategy can be applied to design and construct other photocatalysts for the improvement of photocatalytic performance via an enhanced oxygen molecule activation process.

2 Experimental Section

2.1. Sample preparation

Pristine Bi_2MoO_6 microspheres. The pristine Bi_2MoO_6 microspheres were prepared according to our previous report.[46] In a typical procedure, $Bi(NO_3)_3{\cdot}5H_2O$(1.3 mmol) was dissolved in 13.0 mL of ethylene glycol (EG), then $Na_2MoO_4{\cdot}2H_2O$(0.65 mmol) powder was added under continuous stirring until completely dissolved. Thereafter, 32.5 mL of ethanol was added under magnetic stirring to form a colorless clear liquid. Then, the miscible solution was transferred into a Teflon-lined stainless steel autoclave of 65 mL capacity. The autoclave was sealed and maintained at 160 ℃ for 12 h. After the reaction, the precipitate was separated, washed, and finally dried under vacuum at 60 ℃ overnight. The obtained product was Bi_2MoO_6, which was denoted as BMO.

Au/Bi_2MoO_6 samples (Au/BMO). The Au/Bi_2MO_6 catalysts with SOVs were prepared via a facile chemical reduction-deposition process. Lysine and $NaBH_4$ were used as capping agent and reducing agent, respectively. In a typical process, Bi_2MoO_6(0.50 g) powder was dispersed in deionized water(10 mL), then 0.01 mol·L^{-1} $HAuCl_4$ (5.3 mL) and 0.01 mol·L^{-1} lysine (6.0 mL) were slowly added dropwise. The pH of the mixture was adjusted to 5.0 with 0.1 mol·L^{-1} NaOH solution. Thereafter, the suspension was subjected to ultrasonication for 20 seconds, and 5.3 mL of $NaBH_4$(0.1 mol·L^{-1}) was injected during the sonication. The suspension turned dark in color immediately for the formation of Au colloids and was centrifugal washed with DI water for several times. The product was dried at 60 ℃ in vacuum over night, followed by calcination at 250 ℃ for 2 h to eliminate the lysine residual. The obtained sample were denoted as 2.0 % Au/BMO-A according to the mass ratio of Au to BMO. For comparison, the sample 2.0 % Au/BMO-B was also prepared without calcination. Following the similar procedure, a

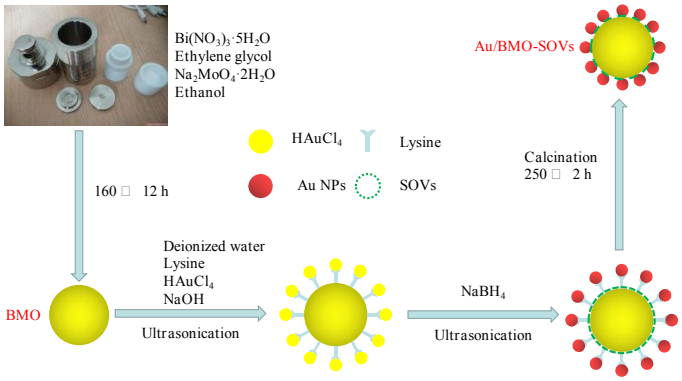

Scheme 1 Schematic diagram of preparation process of Au/BMO-A samples.

series of Au/BMO composites were prepared and denoted as *x* wt%Au/BMO-A (*x* = 0, 1, 2, 4, 6). For comparison, Bi_2MoO_6 with SOVs was also prepared without adding $HAuCl_4$ solution, the obtained sample was denoted as BMO-A. 4wt%Au/Bi_2MoO_6 without SOVs was prepared according to our previously reported photo-reduction process.[47] The obtained sample was denoted as 4wt % Au/BMO-PR. The preparation process of Au/BMO composite is shown in Scheme 1.

2.2 Characterization

Powder X-ray diffraction (XRD) was carried out on a XRD-7000 X-ray diffractometer (Shimadzu, Japan), using Cu Ka radiation (λ = 0.15418 nm) at a scanning rate of 2° min^{-1} in a 2θ range of 20° to 80°. X-ray photoelectron spectroscopy (XPS) valence band (VB-XPS) spectra was recorded on a PHI-5400 X-ray photoelectron spectrometer. Field emission scanning electron microscope (FE-SEM) images were recorded on a JSM-7610F scanning electron microscope. Transmission electron microscopy (TEM) images were obtained on a JEM-2100 electron microscope at an accelerating voltage of 200 kV(JEOL, Japan). In situ electron paramagnetic resonance (EPR) measurement was taken in an Endor spectrometer (JEOL ES-ED3X) at 77 K in liquid nitrogen. The g factor was obtained by taking the signal of manganese as standard. The electron spin resonance (ESR) signals of ·OH and $\cdot O_2^-$ radicals spin-trapped by spin-trap reagent 5, 5-dimethyl-1-pyrroline N-oxide (DMPO) in water were examined on a Bruker model ESR JES-FA200 spectrometer equipped with a quanta-Ray Nd: YAG laser system as the irradiation source (λ > 410 nm). The UV-vis diffuse reflectance spectra (UV-Vis-DRS) were measured with a UV-2550 UV-Vis spectrophotometer (Shimadzu, Japan). Photoluminescence (PL) spectra were measured on an F-4500 spectrophotometer (Hitachi, Japan).

2.3. Time-resolved transient PL measurement

Time-resolved fluorescence decay spectra (TR-PL) were recorded on a FLS920 fluorescence spectrometer (Edinburgh Analytical Instruments, UK) using the time-correlated single photon counting method, excited with a picosecond diode laser (EPL-375) at 377.8 nm, and monitored at 470 nm. A two-exponential function equation was used to fit the decay time, $\tau_{av}=(A_1{\cdot}\tau_1^2+A_2{\cdot}\tau_2^2)/(A_1{\cdot}\tau_1+A_2{\cdot}\tau_2)$. Where τ and A are decay time and the relative magnitude of

View Article Online
DOI: 10.1039/C9CY00570J

components, respectively, and τ_{av} is the average lifetime used for an overall comparison. The results show the fast decay component (τ_1 and A_1) and the slow component (τ_2 and A_2), decaying from the free excited states and the bound excited states, respectively.

2.4. Photoelectrochemical measurement

The Mott-Schottky (MS) curves, photocurrent density versus time (*i-t*) curves and electrochemical impedance spectroscopy (EIS) were measured on a CHI660E electrochemical workstation (Chenhua Instruments, China). The test system comprised a working electrode, a Pt counter electrode, a Ag/AgCl reference electrode , a working electrode and Na_2SO_4 electrolyte (0.1 mol·L^{-1}). The working electrode was prepared from samples fixed on ITO glass. In a typical process, 20 mg photocatalyst was dispersed in 2 mL DI water to get slurry, followed by coating the slurry onto ITO glass and drying at 60 ℃ for 6 h. The area of the electrodes is about 1×2 cm^2. A 400 W halogen lamp (with a UV cutoff filter) is employed as the visible light source.

2.5. Photocatalytic activity

The photocatalytic activity of the samples were evaluated by the degradation of phenol, methyl orange (MO) and rhodamine (RhB). A 300 W halogen lamp was used as sunlight source with 420 nm cutoff filters. First, photocatalyst (200 mg) was dispersed in 200 mL of phenol (10 mg·L^{-1}), MO (10 mg·L^{-1}) or RhB (10 mg·L^{-1}), respectively. The mixture were stirred in dark for 30 min to establish an adsorption/desorption equilibrium. Then, the light source was turned on. During the photocatalytic reaction, 10 mL supernate was sampled at given time intervals, and then photocatalysts was separated through centrifugation. The concentration of pollutant solution was detected by a UV-visible spectrophotometer (Japan, Shimadzu 2550) at the absorption maximum.[49,50] Total organic carbon analyzer (VARIO TOC, Elemental, Germany) was employed for the determining the TOC of phenol solutions.

3 Results and discussion

3.1. Structure and morphology

Fig. 1a shows the XRD patterns of Au/BMO-A heterostructures with different Au contents. The pristine BMO and Au/BMO-A samples are identified as orthorhombic BMO (JCPDS card No.76-2388),[47] indicating that Au NPs have negligible influence on structure of BMO. Two weak diffraction peaks at 38.2 ° and 44.3 ° are observed, which are indexed as (111) plane and (200) plane of Au (JCPDS No. 80-0019), respectively.[51] Furthermore, with the increasing of the Au content, the (131) peak of BMO slightly shifts to a lower angle (Fig. 1b), which may be ascribed to the interaction of Au NPs and BMO surface.

The composition and chemical state of the BMO and Au/BMO heterostructures were confirmed by XPS. Fig. S1a(ESI*) reveals that Au/BMO composite contains Bi, Mo, O, Au and trance amount C element, respectively. The C element should be attributed to the adventitious of XPS instruments itself.[52] Fig. 1c reveal that two characteristic peaks of BMO at around 159 eV and 164.4 eV corresponds to Bi $4f_{7/2}$ and Bi $4f_{5/2}$ of Bi^{3+}. Compared with pristine BMO, the binding energy of 4.0wt% Au/BMO-B and 4.0wt% Au/BMO-A increased to 159.8 eV and 165.1, 159.4 and 164.8 eV, respectively, which can ascribed to the interaction between Au and BMO, and the coexistence of SOVs. [53, 54] According to Fig. S1b(ESI*), the peak at 232.5 eV and 235.6 eV can be assigned to Mo $3d_{5/2}$ and Mo $3d_{3/2}$ of Mo^{6+},[54] and the characteristic peak of 4.0wt%Au/BMO-B and 4.0wt%Au/BMO-A shift to higher binding energy separately to 233.3 eV and 236.3, 233 and 235.9 eV. As shown in Fig. 1(d), the wide asymmetric O1s peaks observed can be fitted into three peaks at 529.7, 530.5 and 531.8 eV for BMO sample, which are attributed to the Bi-O, Mo-O and H-O or adsorbed oxygen, respectively.[55-58] However, the O1s binding energy (Mo-O) of Au/BMO-B and Au/BMO-A have a shift from 530.5 eV to 531.2 eV and 530.95 eV, respectively (Fig. 1d), which are ascribed to the formation of SOVs with a high electron-attracting effect.[59, 60] The Au 4f XPS spectrum presented in Fig. 1Sc(ESI*) indicates that Au 4f spectra of Au/BMO-B is fitted to two peaks at about 84.4 eV and 87.9 eV, which can be assigned to the $4f_{7/2}$ and $4f_{5/2}$ binding energies of Au, suggesting that the Au species in the samples before calcination are presented in the compound state.[61] However, Au 4f binding energy peaks of Au/BMO-A sample have a shift to 84.1 eV and 87.7 eV, which revealed that Au species in the samples were reduced to metallic state after the calcination process.[51, 62]

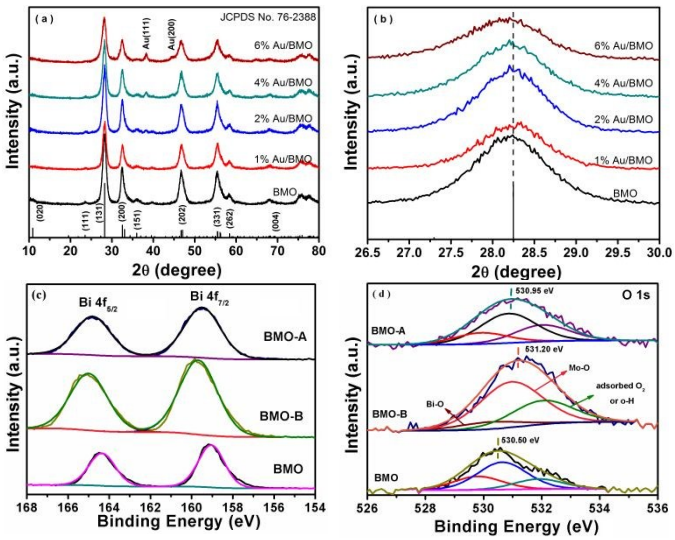

Fig.1 (a) XRD pattern of as-prepared BMO and the series of Au/BMO-A heterostructures, (b) XRD patterns in a 2θ range of 26.5°-30°, (c) XPS spectra of Bi 4f and (d) O 1s for BMO, 4wt%Au/BMO-B and 4wt%Au/BMO-A were before and after calcined at 250°C for 2 h, respectively.

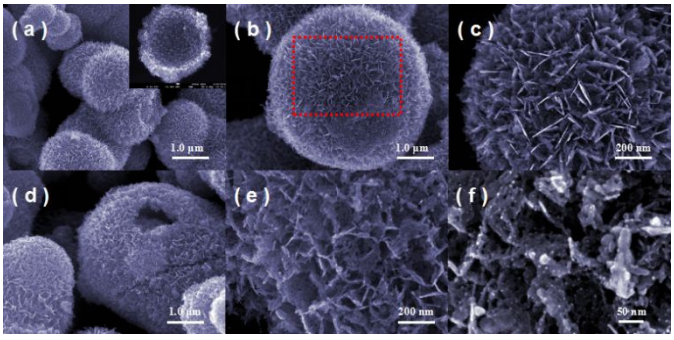

Fig. 2 FE-SEM images of as-prepared (a~c) hollow BMO microsphere, (d~f) 4wt% Au/BMO-A heterostructures.

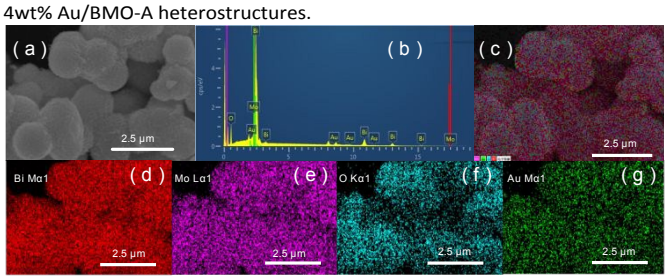

Fig. 3 (a) SEM image of 4wt%Au/BMO microsphere, (b) EDX spectrum of sample Au/BMO, (c) The spatial distribution of all elements in 4wt%Au/BMO-A, and the elemental mapping of (d) Bi, (e) Mo, (f) O and (g) Au in sample 4wt%Au/BMO-A.

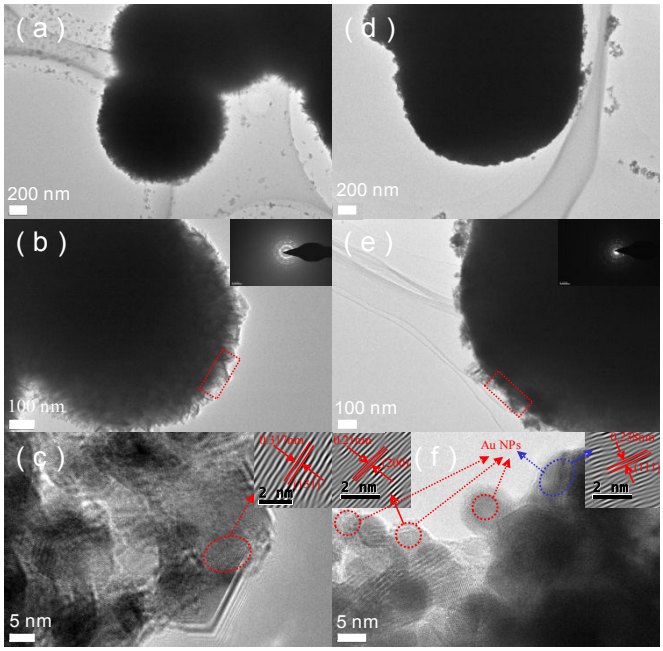

Fig. 4 TEM and HR-TEM images of BMO (a~c) and (e~f) 4wt%Au/BMO-A.

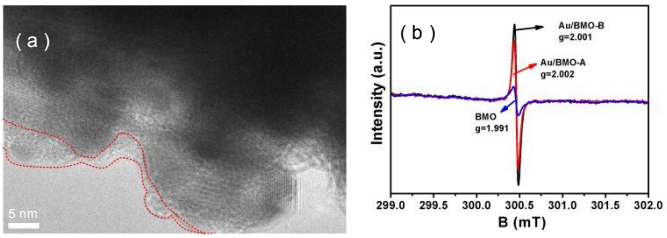

Fig. 5 (a) HR-TEM image of Au/BMO, (b) EPR spectra of BMO, 4wt%Au/BMO-B and 4wt% Au/BMO-A.

According to SEM images shown in Fig. 2(a~c), BMO exhibits a uniform hollow microspheres (insert of Fig. 2a) , which consists of many nanosheets with the thickness of about 10 nm. Likewise, the morphology of 4wt%Au/BMO-A (Fig. 2d~e) is quite similar to that of the hollow BMO microspheres. However, the surface of nanosheets is damaged and blurred after the deposition of Au NPs and calcination at 250 ℃ for 2h (Fig. 2d), which results in the formation of SOVs. In addition, many Au NPs are monodispersed on the secondary nanosheets of BMO microspheres (Fig. 2f). Also, all Au/BMO-A samples exhibit the similar morphology with different Au loading (Fig. S2). The elemental mapping as shown in Fig. 3 (a-b) reveals that 4%Au/BMO-A heterostructure are well agreement with XPS analysis. As shown in Fig. 3(c~g), all the elements are clearly observable and uniformly distributed, revealing that the Au NPs were successfully anchored and highly dispersed onto the surface of BMO microspheres.

To further identify the microstructure of the as-synthesized BMO and Au/BMO-A composite, TEM and HR-TEM were performed. According to Fig.4(a~b), the BMO microspheres consist of many nanosheets with a thickness of about 10 nm. However, HR-TEM images indicate the surface of Au/BMO is relatively smooth (Fig. 4c). The SAED patterns (insert of Fig.4b and Fig.4e) reveal the polycrystalline nature of the BMO and 4wt% Au/BMO-A with the same symmetry. The measured lattice fringes with spacing of 0.317 nm ascribe to the (131) plane of BMO.[53,54] In addition, the interplanar lattice spacing of 0.21 nm and 0.238 nm correspond to the Au (200) and (111) atomic planes, respectively (insert picture in Fig. 4f).[63, 64] It further indicates that Au NPs was deposited on the secondary nanosheets of BMO microspheres.

Although the pristine BMO reveals the perfect lattice fringe (Fig. 4c), the edge of lattice fringe for 4.0wt%Au/BMO-A becomes blurred (Fig. 5a), implying that its surface structure is damaged and SOVs are formed.[60, 65] To further verify the existence of SOVs and monitor the various behaviors of the SOVs, *in-situ* EPR spectra were performed, as shown in Fig. 5b. It indicate that BMO shows a weak EPR signal at g value of 1.991, which may be ascribed to the formation of the SOVs during the solvothermal process. The EPR signal at g = 2.002 for 4wt%Au/BMO-A and 4wt%Au/BMO-B are much higher than pure BMO, as shown in Fig. 5, which is attributed to the unpaired electrons trapped by SOVs.[40, 60, 65-67] Compared to BMO, 4wt%Au/BMO-B also exhibits an obvious increased SOVs signal, indicating that $NaBH_4$ reduction increase the number of SOVs. During the reduction of $HAuCl_4$, the excessive $NaBH_4$ acts as oxygen scavenger for producing the active hydrogen. The strong reduction capability of active hydrogen can remove the oxygen atoms from the surface of BMO, thus forming SOVs.[68] Moreover, the EPR signal of 4wt%Au/BMO-A is slightly lower than that of 4wt%Au/BMO-B due to its calcination in air-rich atmosphere for elimination of lysine.[66] Therefore, it can be concluded that 4wt%Au/BMO-A possess rich SOVs, which can serve as the active sites for improving the carrier transfer efficiency as well as oxygen molecule activation. Also, it could gain the synergistic effect of Au NPs and SOVs in Au/BMO heterostructure.

3.2. Optical properties

The UV-Vis-DRS were employed to investigate the optical properties of BMO and Au/BMO heterostructures. Clearly, the color of Au/BMO changes from yellow to gray and black with the increasing of Au deposition amount (Fig. 6). The BMO microsphere exhibited absorption edge at about 470 nm, corresponding to the intrinsic band-gap transition. When Au NPs were loaded on BMO, the absorption of Au/BMO within visible light range were enhanced and absorption edge became red shift, indicating that the photocatalyst could absorb more photons and be favorable for photocatalytic reaction. In addition, Au/BMO-A samples exhibited an extra absorption peak at about 580 nm (Fig. 6a) due to the absorption of

the Au SPR effect.[40,68,69-71] Furthermore, the intensity of the absorption of the Au SPR effect strengthen with the increasing of

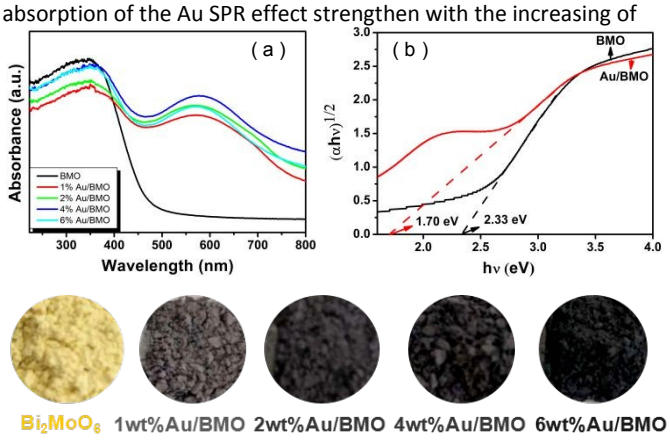

Fig. 6 Optical properties of samples. (a) UV-Vis-DRS spectra; (b)band gap (E_g) of BMO and series of Au/BMO samples.

Au NPs from 1wt% to 4wt%. However, when the deposition amount is more than 5%, the absorption peak change is not obvious. The band-gap energies (E_g) of BMO samples are estimated from a plot of $(\alpha h\nu)^{1/2}$ versus $h\nu$, as displayed in Fig. 6b. The calculated E_g values of BMO and 4wt% Au/BMO-A are around 2.33 and 1.70 eV, respectively (Fig. 6b). The 4wt% Au/BMO-A with Au NPs and SOVs shows more intense light absorption and narrower band gap, indicating that both the planted SOVs and the anchored Au NPs enhance the visible light harvesting.

3.3. Charge-carriers separation efficiency

Due to the photoluminescence (PL) emission originating from the recombination of charge carriers, PL spectrum are often used to investigate the separation and transfer efficiency of e^-/h^+ pairs.[72-75] When 400 nm was used as the excitation wavelength, the PL spectrum of BMO exhibits a strong emission peak at approximately 470 nm(Fig. 7a). However, the PL intensity is dramatically weakened when the Au NPs were deposited. However, with the Au NPs loading amount increasing from 1wt% to 4wt%, the emission peak decreased slightly. Especially, the 4%Au/BMO-A exhibits the weakest PL intensity. It suggests that Au NPs anchored on BMO as well as SOVs can greatly improve the separation efficiency of the photogenerated e^-/h^+ pairs.

To further investigate the e^-/h^+ pairs recombination process for BMO and Au/BMO, the recombination kinetics of photogenerated e^-/h^+ pairs were investigated by TR-FL spectra, as shown in Fig. 7(b). A two-exponential function equation was used to fit the decay time, as listed in Table 1. The photoelectron lifetimes of BMO and 4%Au/BMO are 0.386 and 0.451 ns, respectively, indicating that the synergistic effect of Au NPs and SOVs makes the photoelectron lifetime of the Au/BMO photocatalyst increase.

Furthermore, the effect of Au NPs and SOVs on the carrier concentration and transport BMO was investigated by photocurrent measurements.[76-78] Fig. 7(c) shows the photocurrent density versus time (*i-t*) curves of the samples under visible light ($\lambda \geq 420$ nm) without bias. Evidently, the 4wt%Au/BMO-A composite exhibits a remarkably enhanced photocurrent response in contrast with BMO.The photocurrent intensity of the 4%Au/BMO-A composite is approximately 36-fold larger than that of BMO, revealing that the concentration and transport of the photoexcited charge carriers can be effectively promoted and the superiority of synergism of SOVs

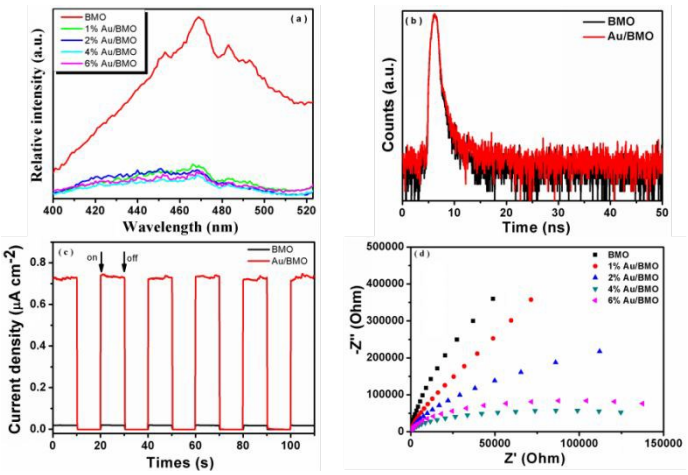

Fig. 7 Charge-carriers separation efficiency of BMO an X wt%Au/BMO(X=1, 2, 4, 6). (a) Photoluminescence spectra, (b) time-resolved fluorescence decay spectra, (c) transient photocurrent response under visible light irradiation and (d) electrochemical impedance spectroscopy (EIS) under visible light.

Table 1 Lifetimes (τ_1 and τ_2) and relative intensities of pure BMO and Au/BMO

samples	τ_1(ns)/Int.(%)	τ_2(ns)/Int.(%)	τ_{av}(ns)	χ^2
BMO	0.19/86.86	1.68/13.14	0.386	1.110
4.0%Au/BMO	0.22/84.39	1.70/15.61	0.451	1.201

and Au can be verified. The electrochemical impedance spectroscopy (EIS) Nyquist plots of pure-BMO and Au/BMO with different amounts of Au are shown in Fig.7(d). It can be seen that 4%Au/BMO-A presents the smallest arc radius, indicating its strongest ability to separate and transfer photogenerated e^-/h^+ pairs.[79,80]

3.4. Photocatalytic performance

The visible-light-responsive activity of BMO and Au/BMO were evaluated by monitoring the degradation of phenol, RhB, and MO. Fig. 8(a) indicated that the degradation of MO was negligible and RhB was about 5% in a blank experiment. However, BMO exhibits photogegradation rate of RhB and MO are 30% and 10% in 25 min, respectively. However, when 4.0wt%Au/BMO-A was employed as photocatalyst, the photocatalytic degradation rate was significantly enhanced, and 100% degradation of MO and RhB could be finished within 100 min and 25 min, respectively. Using BMO and 4.0wt%Au/BMO-A as photocatalysts, the calculated rate constants (k_{app}/ min^{-1}) are 0.00389, 0.04613 min^{-1} for MO, and 0.01515, 0.2229 min^{-1} for RhB, respectively (Fig. 8b). The degradation activities of 4.0 % Au/BMO-A to RhB and MO are approximately 11.9 and 14.7 times higher than BMO, respectively. Furthermore, phenol was used as another model pollutant to investigate the photocatalytic performance of 4.0%Au/BMO-A. Fig. 8c shows the variation of phenol concentration (C/C_0) over photocatalysts against reaction time. The degradation efficiency of phenol was negligible in blank test (without any photocatalyst) and the BMO exhibits 9 % degradation rate after 3 h. However, with the increase of Au loading from 1wt% to 4wt% in the Au/BMO, the degradation rate of

phenol was significantly enhanced. But when further increased the Au loading, the photocatalytic activity decreased. It is because the more Au deposition conversely occupies the active sites of the catalyst surface, which results in the decreasing of the photocatalyst activity. According to the first-order kinetics model,[81] the apparent rate constant(k_{app}/min^{-1}) are 0.0339, 0.2087, 0.4212, 0.5095 and 0.2424 min^{-1} for pure-BMO, 1wt%Au/BMO, 2wt%Au/BMO, 4wt%Au/BMO and 6wt%Au/BMO, respectively (Fig. 8d). It can be seen that the k_{app} value of 4wt%Au/BMO-A is much higher than others, which is approximately 15 times higher than pure-BMO. Fig. 8(e) indicated that the absorption characteristic of phenol peak at 270 nm obviously decreases after 180 min irradiation. As shown in Fig. S3, both SOVs planting and Au NPs anchoring can enhance the photocatalytic activity of pristine Bi_2MoO_6 for phenol degradation. Furthermore, 4wt%Au/Bi_2MoO_6 with SOVs(4wt%Au/BMO-A) exhibited the better photocatalytic activity for phenol degradation than that of 4wt%Au/Bi_2MoO_6 without SOVS(4wt%Au/BMO-PR) and Bi_2MoO_6 with SOVs(BMO-A). The enhanced photocatalytic activity of 4wt%Au/BMO-A is attributed to the synergistic effect between the SOVs, Au NPs and Bi_2MoO_6, which not only narrows the band gap, improving the visible light response ability, but also facilitates the formation of Schottky barriers between Au NPs and Bi_2MoO_6. The Au/Bi_2MoO_6 interface allows only the movement of electrons from the Bi_2MoO_6 to Au NPs and hinders electron transfer back across the Schottky barrier, and thereby prevents from the recombination of the photogenerated electron-hole pairs.[54]

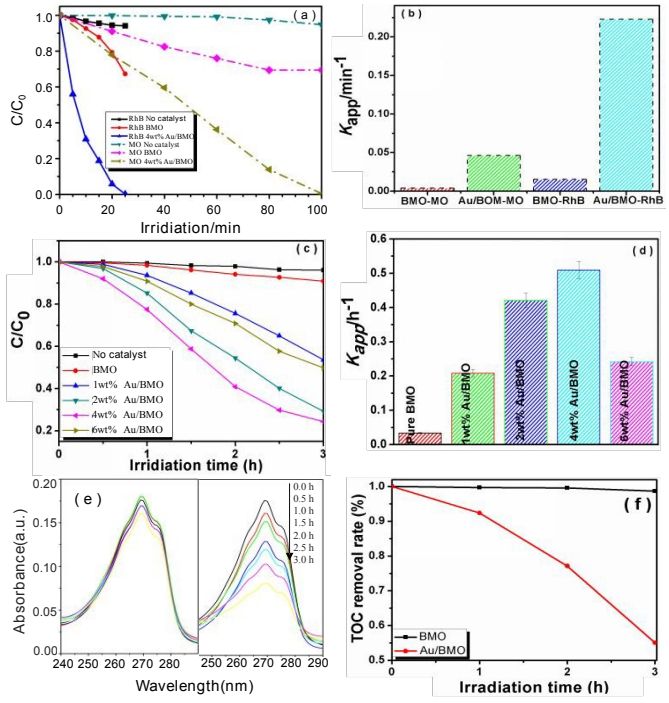

Fig. 8 (a) Photocatalytic degradation efficiency of RhB or MO by BMO and 4wt% Au/BMO, (b) The apparent rate constant (k_{app}/min^{-1}) of the photodegradation of RhB and MO using different catalysts, (c) Photocatalytic degradation efficiency of phenol by BMO and *x*wt%Au/BMO-A(*x*=1, 2, 4, 6), (d) The apparent rate constants(k_{app}/h^{-1}) of the photodegradation of phenol using different catalysts, and (e) The change of the absorption spectra of photodegradated phenol with increasing irradiation time under visible light using BMO (left) and 4wt% Au/BMO-A (right), (f) TOC changes during the course of phenol photodecomposition in the presence of BMO and 4wt%Au/BMO-A under visible light radiation.

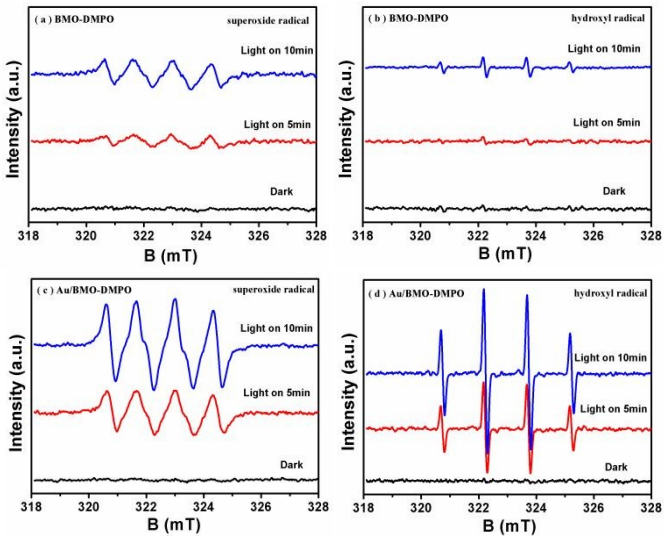

Fig. 9 DMPO spin-trapping ESR spectra of photocatalysts in water for (a~b) BMO; (c~d)4wt%Au/BMO-A.

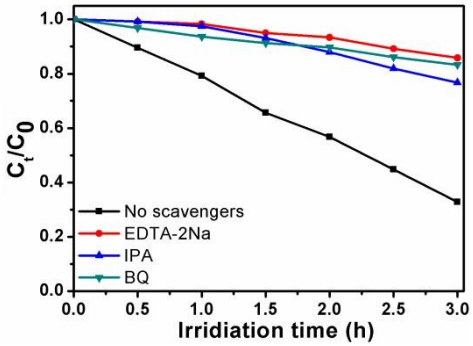

Fig. 10 Photogenerated carrier trapping in the system of photodegradation of phenol by 4wt%Au/BMO-A under visible light irradiation (λ> 420 nm).

To further investigate the mineralization rate of phenol, the total organic carbon (TOC) was detected (Fig. 8f). The mineralization yield of 4% Au/BMO-A reaches as high as 45% after 3h of irradiation, while that of BMO is only 1.3%, proving the enhanced photocatalytic performance of the former.

3.5. Enhanced Oxygen molecule activation mechanism

To further reveal the possible mechanism of oxygen molecule activation, the ESR spin trapping technique were performed to identify the main active species under visible light irradiation as shown in Fig. 9. The intensity of ·OH and $\cdot O_2^-$ radical signals is enhanced with the irradiation time prolonging, indicating that the formation of radical during the photodegradation process. Importantly, ESR signal of ·OH and $\cdot O_2^-$ intensities for 4%Au/BMO-A are significantly enhanced compared to BMO. It reveals that Au NPs deposition and SOVs can increase the separation efficiency of e^-/h^+ pairs, and thereby promotes the oxygen activation efficiency as well as photocatalytic activity of BMO. Moreover, the active species trapping experiments during the photodegradation of phenol over 4%Au/BMO-A were also conducted. Ethylenediaminetetraacetic

View Article Online
DOI: 10.1039/C9CY00570J

acid disodium salt (EDTA-2Na), isopropanol (IPA) and benzoquinone (BQ), were utilized as the scavengers of h^+, ·OH and $\cdot O_2^-$, respectively.[82] As shown in Fig. 10, BQ and IPA hindered the photocatalytic degradation of phenol, while EDTA-2Na evidently suppressed the photocatalytic degradation efficiency of phenol. Thus, it could be concluded that both ·OH and $\cdot O_2^-$ were main active species in the phenol photodecomposition process. Meanwhile, phenol could be direct oxidized degradation by photogenerated h^+ of Au/BMO.

In order to further elucidate the oxygen molecule activation mechanism, conduction band (CB) and valence band (VB) positions of all the samples were examined, as shown in Fig. S4(ESI*) and Fig. S5(ESI*). From Fig. S4(ESI*), it can be seen that both BMO and Au/BMO show a positive slop, indicating that they are all n-type semiconductors. The flat band potentials of BMO and Au/BMO are -0.33 and -0.28 V, respectively, versus the Ag/AgCl electrode, which corresponds to -0.11 and -0.06 V versus the normal hydrogen electrode (NHE).[83,84] Fig. S5(ESI*) exhibits the VB-XPS spectrum of BMO and Au/BMO. It reveals that the energy gap between Fermi level (E_f) and valence band are 2.00 and 1.32 V for BMO and 4wt% Au/BMO, respectively.[85] It has been reported that the flat band potential of n-type semiconductor equals the Fermi level.[36-38] Hence, the calculated VB positions of BMO and Au/BMO are 1.89 and 1.26 V, respectively. The CB positions of both BMO and 4wt%Au/BMO are calculated based on the band gaps to be -0.44 eV, respectively, which are higher than $O_2/\cdot O_2^-$ (-0.33 V vs NHE).[86,87] Moreover, the band diagrams of BMO and Au/BMO are shown in Fig. S6(ESI*).

Based on the above results, a schematic diagram for the charge separation and oxygen molecule oxygen mechanism over SOVs and plasmonic Au NPs co-modified BMO photocatalyst is proposed and illustrated in Scheme 2, thereby, the mechanism for the enhanced photocatalytic activity under visible light is suggested. SOVs is a shallow defect, which may near the minimum conduction band (CBM) or above the valence band maximum (VBM).[81,86] As manifested in our previous works, the existence of SOVs would induce the formation of subbands above the VB of BMO.[88] The enhancement of photocatalytic activity for the Au/BMO heterostructures compared to pure BMO can be interpreted as follows. During the visible light irradiation, the Au/BMO can be excited to produce e^-/h^+ pairs and the photogenerated e^- in the CB could transfer to Au NPs,because the Fermi level of BMO is -0.11 V vs NHE,[31] lower than that of gold (0.45 V vs NHE).[48] Consequently, a Schottky barrier height of 0.56 V is generated at the Au/BMO interface. Additionally, when Au NPs are deposited on the surface of BMO, due to the Fermi level equilibrium between BMO and Au NPs, Schottky barriers formed at a Au-BMO junction.[64,89] This unique Au-BMO interface allows the e^- transfer from BMO to Au NPs and hinders its transfer back across the Schottky barrier, and thereby prevents the recombination of the photogenerated e^-/h^+ pairs. Thus, the photogenerated e^- from the CB of BMO tend to transfer to the Au surface due to the surface electric near field produced by the SPR effect of Au NPs, which facilitates the e^-/h^+ separation on the BMO. Therefore, photogenerated e^- can survive for a period of time in the current research, which will play a vital role in the photocatalytic process. Additionally, due to the lower CB (-0.44 eV vs NHE) voltage of BMO than the redox potential of $O_2/\cdot O_2^-$ (-0.33 eV vs NHE), which can be trapped by O_2 to further form $\cdot O_2^-$ and it further binds to the proton to form ·OH. In addition, the phenol could be directly degraded by the h^+ from the VB of BMO. Hence, for Au/BMO, synergistic effect of SOVs and surface plasmonic Au greatly accelerate its catalytic performance for the phenol degradation under visible light irradiation.

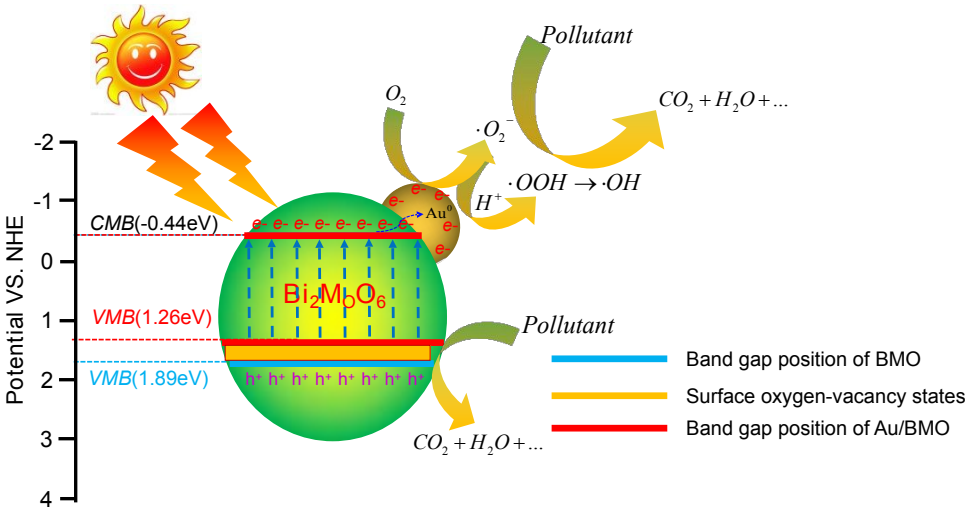

Scheme 2 Schematic illustration of hole/electron separation and transfer process for the Au/BMO photocatalysts under visible light irradiation.

Conclusions

In summary, SOVs and Au NPs co-modification BMO photocatalyst has been rationally designed and successfully fabricated via a facile reduction–deposition method. Simultaneously planting SOVs and depositing Au NPs on the surface of BMO can greatly improve the separation efficiency of photogenerated carriers as well as enlarge the visible-light responsive region, thereby enhance the

oxygen molecule activation efficiency. The as-fabricated Au/BMO heterostructure exhibited superior tphotocatalytic performance for phenol and dyes degradation, in which the 4% Au/BMO composite exhibits the optimal efficiency under visible light irradiation. The SPR effect of Au NPs and surface oxygen vacancy plays the important roles in the enhancement of photocatalytic activity. Dual synergistic effect of the surface oxygen vacancy, the SPR of Au nanoparticles, and the unique metal-semiconductor junction effectively improves the separation and migration of photogenerated electrons and holes and simultaneously represses the recombination of electrons and holes, resulting in the high photocatalytic performance of Au/BMO. The present work provides an effective strategy to improve the oxygen molecule activation efficiency through dual synergistic effect of SOVs and metal NPs of SPR effect.

Conflicts of interest

There are no conflicts to declare.

Acknowledgments

This work was supported by the National Natural Science Foundation of China (No. 21663030, 21666039) and the Open Project of State Key Laboratory of Organic-Inorganic Composites Beijing Key Laboratory, Beijing University of Chemical Technology Beijing(No.oic-201901009) and the Project of Science & Technology Office of Shaanxi Province (No. 2018TSCXL-NY-02-01, 2015SF291) and the Project of Yan'an Science and Technology Bureau (No. 2018KG-04).

References

[1] J. J. Wang, L. Tang, G. M. Zeng, Y. N. Liu, Y. Y. Zhou, Y. C. Deng, J. J Wang, and B. Peng, *ACS Sustainable Chem. Eng*., 2017, **5**, 1062-1072.

[2] F. Y. Ma, Q. L. Yang, Z. J. Wang, Y. H. Liu, J. J. Xin, J. J. Zhang, Y. T. Hao and L.Li, *RSC Adv*., 2018, **8**, 15853-15862.

[3] S. N. Lou, J. Scott, A. Iwase, R. Amala and Y. H. Ng, *J. Mater. Chem. A*, 2016, **4**, 6964-6971.

[4] C. N. Ri, S.G. Kim, K. S. Ju, H. S. Ryo, C. H. Muna and U H. Kima, *RSC Adv*., 2018, **8**, 5433-5440.

[5] L. B. Jiang, X. Z. Yuan, Y. Pan, J. Liang, G. G. Zeng, Z. B. Wu and H. Wang, *Appl. Catal. B:Environ*., 2017, **217**, 388-406.

[6] H. Li, F. Qin, Z. P. Yang, X. M. Cui, J. F. Wang and L. Z. Zhang, *J. Am. Chem. Soc*., 2017, **139,** 3513-3521.

[7] T. Chen, Q. Hao, W. J. Yang, C. L. Xie, D. M. Chen, C. Ma, W. Q. Yao and Y. F. Zhu, *Appl. Catal. B: Environ*., 2018, **237**, 442-448.

[8] Y. X. Chen, T. T. Shi, P. Y. Liu, X. G. Ma, L. L. Shui, C. Q. Shang, Z. H. Chen, X. Wang, K. Kempa and G. F. Zhou, *J. Mater. Chem. A*, 2018, **6**, 19167-19175.

[9] Y. Y Zhu, Y. J. Wang, Q. Ling and Y. F. Zhu, *Appl. Catal. B:Environ*., 2017, **200**, 222-229.

[10] Y. Y Zhu, Q. Ling, Y. F. Liu, H. Wang and Y. F. Zhu, *Appl. Catal. B:Environ*., 2016, **187**, 204-211.

[11] B. Y Xu, Y. An, Y. Y. Liu, X. Y. Qin, X. Y. Zhang, Y. Dai, Z. Y. Wang, P. Wang, M. H. Whangbo and B. B. Huang, *J. Mater. Chem. A*, 2017, **5**, 14406-14414.

[12] J. B. Zhong, Y. K. Zhao, L. Y. Ding, H. W. Ji, W. H. Ma, C. C. Chen and J. C. Zhao, *Appl. Catal. B: Environ*., 2018, **241**, 514-520.

[13] L. Xue, D. Xu, Y. Xi, R. Zhao, L. N. Zhao, M. S. Song, H. J. Zhai, G. B. Che and L. M. Chang, *Colloids and Surfaces A: Physicochem. Eng. Aspects,* 2017, **513**, 117-124.

[14] H. P. Li, Q. H. Deng, J. Y. Liu, W. G. Hou, N. Du, R. J. Zhang and X. T. Tao, *Catal. Sci. Technol*., 2014, **4**, 1028-1037.

[15] X. Li, M. Y. Su, G. F. Zhu, K. G. Zhang, X. Zhang and J. Fan, *Dalton Trans*., 2018, **47**, 10046-10056.

[16] Y. J. Chen, G. H. Tian, Y. H. Shi, Y. T. Xiao and H. G. Fu, *Appl. Catal. B: Environ*., 2015, **164**, 40-47.

[17] Z. Dai, F. Qin, H. P. Zhao, J. Ding, Y. L. Liu and R. Chen, *ACS Catal*., 2016, **6**, 3180−3192.

[18] J. X. Low, J. G. Yu, M. Jaroniec, S. Wageh and A. A. Al-Ghamdi, *Adv. Mater*., 2017, **29**, 1601694.

[19] Q. L. Xu, B. Cheng, J. G. Yu and G. Liu, Carbon, 2017, **118**, 241-249.

[20] Y. Nosaka and A. Y. Nosaka, *Chem. Rev*., 2017, **117**, 11302-11336.

[21] Y. L. Jia, Y. H. Lin, Y. Ma and W. B. Shi, *Mater. Lett*., 2018, **234**, 83-86.

[22] J. Tian, P. Hao, N. Wei, H. Z. Cui and H. Liu, *ACS Catal*., 2015, **5**, 4530-4536.

[23] Y. Ma, Y. L. Jia, L. N. Wang, M. Yang, Y. P. Bi and Y. X. Qi, *J. Power Sources*, 2016, **331**, 481-486.

[24] J. L. Long, S. C. Wang, H. J. Chang, B. Z. Zhao, B. T. Liu, Y. G. Zhou, W. Wei, X. X. Wang, L. Huang and W. Huang, *Small*, 2014, **10**, 2791-2795.

[25] S. Yuan, Y. Zhao, W. B. Chen, C. Wu, X. Y. Wang, L. N. Zhang and Q. Wang, *ACS Appl. Mater. Interfaces*, 2017, **9**, 21781-21790.

[26] Y. Ma, Y. L. Jia, Z. B. Jiao, M. Yang, Y. X. Qi, and Y. P. Bi, *Chem. Commun*., 2015, **51**, 6655-6658.

[27] Y. Chen, W. Y. Yang, S. Gao, C. X. Sun and Q. Li, *ACS Appl. Nano Mater*., 2018, **1**, 3565-3578.

[28] Y. S. Li, Z. L. Tang, J. Y. Zhang and Z. T. Zhang, *J. Phys. Chem. C*, 2016, **120**, 9750−9763.

[29] Y. H. Lv, Y. F.Liu, Y. Y. Zhu and Y. F. Zhu, *J. Mater. Chem. A*, 2014, **2**, 1174-1182.

[30] G. M. Wang, H. Y. Wang, Y. C. Ling, Y. C. Tang, X. Y. Yang, R. C. Fitzmorris, C. C. Wang, J. Z. Zhang and Y. Li, *Nano Lett*., 2011, **11**, 3026-3033.

[31] J. Chen, Z. Y. Ding, C. Wang, H. S. Hou, Y. Zhang, C. W. Wang, G. Q. Zou and X. B. Ji, *ACS Appl. Mater. Interfaces*, 2016, **8**, 9142-9151.

[32] D. Chen, F. Niu, L. S. Qin, S. Wang, N. Zhang and Y. X. Huang, *Sol. Energ. Mat. Sol. C*, 2017, **171**, 24-32.

[33] H. S. Kim, J. B. Cook, H. Lin, J. S. Ko, S. H. Tolbert, V. Ozolins and B. Dunn, *Nat. Mater*., 2017, **16**, 454-460.

[34] M. L. Guan, C. Xiao, J. Zhang, S. J. Fan, R. An, Q. M. Cheng, J. F. Xie, M. Zhou, B. J. Ye and Y. Xie, *J. Am. Chem. Soc*., 2013, **135**, 10411-10417.

[35] S. J. Wu, J. W. Xiong, J. G. Sun, Z. D. Hood, W. Zeng, Zh. Z. Yang, L. Gu, X. X. Zhang and S. Z. Yang, *ACS Appl. Mater. Interfaces*, 2017, **9**, 16620-16626.

[36] F. Wang, D. Chen, N. Zhang, S. Wang, L. S. Qin, X. G. Sun and Y. X. Huang, *J. Colloid Interf. Sci*., 2017, 508, 237-247.

[37] J. S. Cai, J. Y. Huang, Y. K. Lai, *J. Mater. Chem. A*, 2017, **5**, 16412-16421.

[38] C. L. Yu, Y. Bai, J. C. Chen, W. Q. Zhou, H. B. He, J. C. Yu, L. H. Zhu and S. S. Xue, *Sep. Purif. Technol*., 2015, **154**, 115-122.

[39] R.M. Mohamed and F.M. Ibrahim, *J. Ind. Eng. Chem*., 2015, **22**, 28-33.

[40] Z. K. Zheng, B. B. Huang, X. Y. Qin, X. Y. Zhang, Y. Dai and M. H. Whangbo, *J. Mater. Chem*., 2011, **21**, 9079-9087.

[41] Y. L. Qi, Y. F. Zheng and X. C. Song. *J. Alloy. Compd*., 2017, **726**, 1147-1154.

[42] P. Li, Z. Wei, T. Wu, Q. Peng and Y. D. Li, J. *Am. Chem. Soc*., 2011, **133**, 5660-5663.

[43] C. G. Zhou, S. M. Wang, Z. Y. Zhao, Z. Shi, S. C. Yan and Z. G. Zou, *Adv. Funct. Mater*., 2018, 1801214.

[44] X. Q. Yan, X. H. Zhu, R. H. Li and W. X Chen, *J. Hazard. Mater*, 2016, **303**, 1-9.

[45] H. L. Tan, A. Suyanto, A. T. De Denko, W. H. Saputera, Amal, F. E. Osterloh and Y. H. Ng, *Part. Part. Syst. Charact*., 2017, **34**, 1600290.

[46] D. J. Wang, H. D. Shen, L. Guo, C. Wang, F. Fu and Y. C. Liang, *RSC Adv*., 2016, **6**, 71052-71060.

[47] D. J. Wang, G. L. Xue, Y. Z. Zhen, F. Fu and D. S. Li, *J. Mater. Chem*., 2012, 22, 4751-9782.

[48] J. Yang, X. H. Wang, Y. M. Chen, J. Dai and S. H. Sun, *RSC Adv*., 2015, **5**, 9771-9782.

[49] Y. L. Jia, Y. Ma, J. Z. Tang and W. B. Shi, *Dalton Trans*., 2018, **47**, 5542-5547.

[50] J. J. Wang, L. Tang, G. M. Zeng, Y. N. Liu, Y. Y. Zhou, Y. C. Deng, J. J Wang and B. Peng, *ACS Sustainable Chem. Eng*., 2017, **5**, 1062-1072.

[51] W. B. Li, C. Feng, S. Y. Dai, J. G. Yue, F. X. Hua and H. Hou, *Appl. Catal. B: Environ*., 2015, **168**, 465-471.

[52] T. P. Hu, Y. Yang, K. Dai, J. F. Zhang and C. H. Liang, *Appl. Surf. Sci*., 2018, **456**, 473-481.

[53] D. J. Wang, H. D. Shen, L. Guo, F. Fu and Y. C. Liang, *New J. Chem*., 2016, **40**, 8614-8624.

[54] D. J. Wang, H. D. Shen, L. Guo, C. Wang, F. Fu and Y. C. Liang, *Appl. Surf. Sci*., 2018, **436**, 536-547.

[55] Y. Yin, F. Li, Q. F. Zhan, D. M. Jiang and R. Z. Chen. *Mater. Res. Bull*., 2018, **103**, 47-54.

[56] Z. J. Zhu, Y. Li , C. M. Wang, L. J. Liang, D. Yu, J. Sun, P. Gao and B. J. Liu, *Mater. Let*., 2018, **227**, 296–300.

[57] X. Li, M. Y. Su, G. F. Zhu, K. G. Zhang, X. Zhang and J. Fan, *Dalton Trans*., 2018, 47, 10046-10056.

[58] H. D. Li, W. J. Li, X. T. Liu, C. J. Ren, X. Miao and X. Y. Li, *Appl. Surf. Sci*., 2019, **463**, 556-565.

[59] Y. H. Lv, W. Q. Yao, R. L. Zong and Y. F. Zhu, *Sci. Rep*., 2016, **6**, 19347.

[60] J. Tian, Z. w. Chen , X. Y. Deng , Q. Sun , Z.Y. Sun and W. B. Li, *Appl. Surf. Sci*., 2018, **453**, 373-382.

[61] Y. C. Wei, J. Liu, Z. Zhao, Y. S. Chen, C. M. Xu, A. J. Duan, G. Y. Jiang and H. He, *Angew. Chem. Int. Ed*., 2011, **50**, 2326-2329.

[62] S. H. Xie, J. G. Deng, S. M. Zang, H. G. Yang, G. S. Guo, H. Arandiyan and H. X. Dai, *J. Catal*., 2015, **322**, 38-48.

[63] M. Wang, Q. T. Han, L. Li, L. Q. Tang, H. J. Li, Y. Zhou and Z. G. Zou, Nanotechnology, 2017, **28**, 274002.

[64] X. L. Hu, J. Tian, Y. J. Xue, Y. J. Li and H. Z. Cui, *ChemCatChem*, 2017, **9**,1511-1516.

[65] Y. X. Wang, W. J. Yang, X. J. Chen and J. Wang, Y. F. Zhu, *Appl. Catal. B: Environ*., 2018, **220**, 337-347.

[66] Y. T. Wang, J. M. Cai, M. Q. Wu, J. H. Chen, W. Y. Zhao, Y. Tian, T. Ding, J. Zhang, Z. Jiang and X. G. Li, *Appl. Catal. B: Environ*., 2018, **239**, 398-407.

[67] Z. Wei, Y. F. Liu, J. Wang, R. L. Zong, W. Q. Yao, J. Wang and Y. F. Zhu, *Nanoscale*, 2015, **7**, 13943-13950.

[68] H. Q. Tan, Z. Zhao, W. B. Zhu, E. N. Coker, B. S. Li, M. Zheng, W. X. Yu, H. Y. Fan and Z. C. Sun, *ACS Appl. Mater. Interfaces*, 2014, **6**, 19184−19190.

[69] Y. F. Zhang and S. J. Park, *J. Catal*., 2017, **355**, 1-10.

[70] K. M. Parida,N. Sahu, A. K. Tripathi and V. S. Kamble, *Environ. Sci. Technol*., 2010, **44**, 4155-4160.

[71] Y. X. Zhou, P. F. Lv, W. Zhang, X. D. Meng, H. He, X. H. Zeng and X. S. Shen, *Appl. Surf. Sci*., 2018, **457**, 925-932.

[72] Y. He, Y. H. Zhang, H. W. Huang, N. Tian and Y. Luo, *Inorg. Chem. Commun*., 2014, **40**, 55-58.

[73] H. D. Li, W. J. Li, F. Z. Wang, X. T. Liu, C. J. Ren and X. Miao, *Appl. Surf. Sci*., 2018, **427**, 1046-1053.

[74] Z. Z. Li, X. C. Meng and Z. S. Zhang, *Catal. Today*, 2018, **315**, 67-78.

[75] C. Liang, C. G. Niu, H. Guo, D. W. Huang, X. J. Wen, S. F. Yang and G. M. Zeng, *Catal. Sci. Technol*., 2018, **8**, 1161-1175.

[76] H. Xu, J. Yan, Y. G. Xu, Y. H. Song, H. M. Li, J. X. Xia, C. J. Huang and H. L. Wan, *Appl. Catal. B: Environ*., 2013, **129**, 182-193.

[77] Y. Z. Hong, E. L. Liu, J. Y. Shi, X. Lin, L. Z. Sheng, M. Zhang, L. Y. Wang and J. H. Chen, *Int. J. Hydrogen Energy,* 2019, **44**, 7194-7204.

[78] G. Ge, M. Liu, C. Liu, W. Zhou, D. F. Wang, L.Q. Liu and J. H. Ye, *J. Mater. Chem. A*, 2019, **7**, 9222- 9229.

[79] D. Liu, W. B. Cai, Y.G. Wang and Y. F. Zhu. *Appl. Catal. B: Environ*., 2018, **236**, 205-211.

[80] Y. Y. Wang,W. J. Jiang,W. J. Luo, X. J. Chen and Y. F. Zhu, *Appl. Catal. B: Environ*., 2018, **237**, 633-640.

[81] Y. Wang, G. Q. Tan, T. Liu, Y. N. Su, H. J. Ren, X. L. Zhang, A. Xia, L. Lv and Yun Liu, *Appl. Catal. B: Environ*., 2018, **234**, 37-49.

[82] L. Q. Jing, Y. G. Xu, S. Q. Huang, M. Xie, M. Q. He, H. Xu, H. M. Li and Q. Zhang, *Appl. Catal. B: Environ*., 2016, **199**, 11-22.

[83] H. W. Huang, Y. He, X. W. Li, M. Li, C. Zeng, F. Dong, X. Du, T. Zhang and Y. H. Zhang, *J. Mater. Chem. A*, 2015, **3**, 24547-24556.

[84] Y. Gong, X. Quan, H. T. Yu, S. Chen and H. M. Zhao, Appl. Catal. B-Environ., 2018, 237, 947-956.

[85] H. F. Li, H. T. Yu, X. Quan, S. Chen and Y. B. Zhang, *ACS Appl. Mater. Interfaces*, 2016, **8**, 2111-119.

[86] Y. Gong, X. Quan, H. T. Yu, S. Chen and H. M. Zhao, *Appl. Catal. B: Environ*., 2018, **237**, 947-956.

[87] Y. H. Lv, Y. Y. Zhu and Y. F. Zhu, *J. Phys. Chem. C*, 2013, **117**, 18520-18528.

[88] X. B. Zhu, C. Jin, X. S. Li, J. L. Liu, Z. G. Sun, C. Shi, X. G. Li and A. M. Zhu, *ACS Catal*., 2017, **7**, 6514-6524.

[89] F. Fu, H. D. Shen, X. Sun, W. W. Xue, A. Shoneye, J. N. Ma, L. Luo, D. J. Wang, J. G.Wang, J. W. Tang, *Appl. Catal. B: Environ*., 2019, **247**,150-162.

ARTICLE Journal Name

View Article Online
DOI: 10.1039/C9CY00579J

A table of contents entry

Ultrafine Au Nanoparticles Anchored on Bi_2MoO_6 with Abundant Surface Oxygen Vacancies for Efficient Oxygen Molecule Activation

Li Guo,[a] Qiang Zhao,[a] Huidong Shen,[a] Xuanxuan Han[a], Kailai Zhang[a], Danjun Wang *[a], Feng Fu*[a] and Bin Xu*[b]

[a] Shaanxi Key Laboratory of Chemical Reaction Engineering, School of Chemistry & Chemical Engineering, Yan'an University, Yan'an 716000, China.

[b] State Key Laboratory of Organic-Inorganic Composites Beijing Key Laboratory of Electrochemical Process and Technology for Materials, Beijing University of Chemical Technology, Beijing 100029, China.

Summary:

Au NPs were anchored on Bi_2MoO_6 with rich SOVs to improve O_2 activation for photocatalytic degradation of phenol and dye.

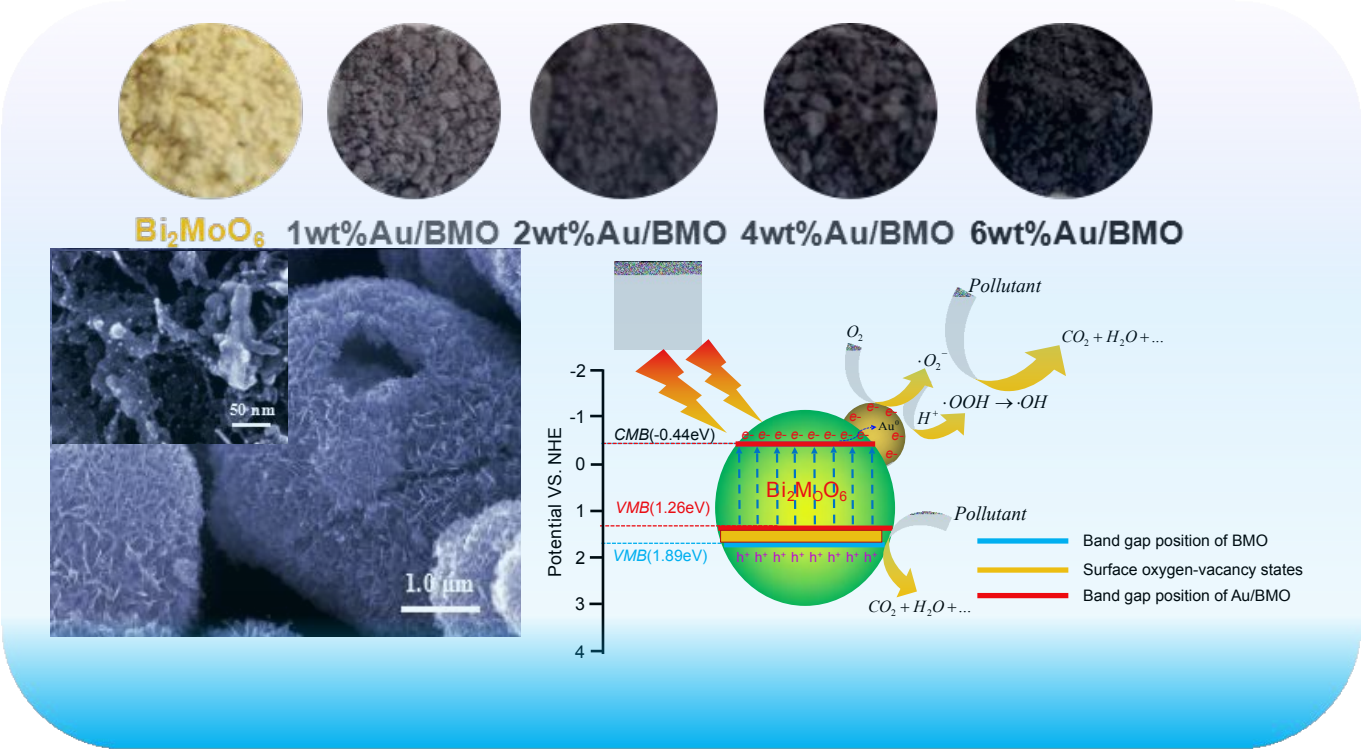

Catalysis Science & Technology

View Article Online
DOI: 10.1039/C9CY00579J

ARTICLE